RESEARCH ARTICLE

ADVANCED MATERIALS
www.advmat.de

Unlocking Efficient Alkaline Hydrogen Evolution Through Ru–Sn Dual Metal Sites and a Novel Hydroxyl Spillover Effect

Zhen-Tong Yan, Shi Tao, Juan Wang, Xiu-Li Lu, and Tong-Bu Lu**

Alkaline hydrogen evolution reaction (HER) has great potential in practical hydrogen production but is still limited by the lack of active and stable electrocatalysts. Herein, the efficient water dissociation process, fast transfer of adsorbed hydroxyl and optimized hydrogen adsorption are first achieved on a cooperative electrocatalyst, named as Ru–Sn/SnO_2 NS, in which the Ru–Sn dual metal sites and SnO_2 heterojunction are constructed based on porous Ru nanosheet. The density functional theory (DFT) calculations and in situ infrared spectra suggest that Ru–Sn dual sites can optimize the water dissociation process and hydrogen adsorption, while the existence of SnO_2 can induce the unique hydroxyl spillover effect, accelerating the hydroxyl transfer process and avoiding the poison of active sites. As results, Ru–Sn/SnO_2 NS display remarkable alkaline HER performance with an extremely low overpotential (12 mV at 10 mA cm^{-2}) and robust stability (650 h), much superior to those of Ru NS (27 mV at 10 mA cm^{-2} with 90 h stability) and Ru–Sn NS (16 mV at 10 mA cm^{-2} with 120 h stability). The work sheds new light on designing of efficient alkaline HER electrocatalyst.

1. Introduction

Alkaline water electrolysis has been regarded as an economical route for large-scale hydrogen production with zero emissions.[1–3] However, the hydrogen evolution reaction (HER) under alkaline condition is sluggish because the used proton is derived from water dissociation, while the proton for acidic HER is direct access from media.[4–6] Specifically, the process of alkaline HER includes the Volmer process ($H_2O + e^- \rightleftharpoons H^* + OH^-$), which involves the water dissociation ($H_2O \rightleftharpoons H^* + {}^*OH$) as well as the desorption of adsorbed hydroxyl (${}^*OH + e^- \rightleftharpoons OH^-$), and the subsequent Heyrovsky or Tafel step (hydrogen combination process).[7–9] To overcome the slow HER kinetics under alkaline condition, most developed catalysts mainly concentrate on accelerating the water dissociation and regulating the hydrogen adsorption.[10–12] However, the transfer of adsorbed hydroxyl (*OH), which also plays a critical role in overall HER activity, is hardly considered. When the binding energy between active sites and *OH is too strong during the initial Volmer process, the active sites would be poisoned due to the accumulation of *OH, which could decrease the rate of HER and cause the deactivation of the electrocatalyst.[13–15] In this regard, designing a highly active and stable electrocatalyst for alkaline HER by collectively promoting water dissociation, accelerating *OH transfer, and optimizing hydrogen adsorption is urgently needed and is extremely challenging.

As is well known, Ru-based catalyst has been widely applied in alkaline HER due to its relatively low price and high catalytic performance for water splitting with strong metal-hydrogen bonds.[16–18] During the past decades, to improve the performance of Ru-based catalysts, various strategies have been developed to optimize hydrogen adsorption and accelerate water dissociation.[19–21] For example, Guo and co-workers reported that Cu-doped heterogeneous Ru/$RuSe_2$ with optimized H and H_2O adsorption strength demonstrate highly efficient performance for alkaline HER due to a synergistic effect of the unique heterointerface structure and Cu doping.[22] By combining highly oxophilic Ce single atoms and fully-exposed Ru nanoclusters on N functionalized carbon support, the mass activity for alkaline HER could achieve −10.1 A mg^{-1} at −0.05 V, which is superior to most of the reported Ru-based catalysts.[23] Despite all the progress, a simultaneous realization of high catalytic activity and stability for alkaline HER on Ru-based catalyst is still challenging.

As reported, constructing dual metal sites has shown great promise in complicated reaction. For example, it is reported that the atomic copper–iron dual-site bridged by an axial oxygen atom (O–Fe–N_6–Cu) on N-doped carbon support demonstrates high catalytic performance for synthesis of NH_3 by electrocatalytic reduction of NO due to the improved rate-determining step and

---

Z.-T. Yan, J. Wang, X.-L. Lu, T.-B. Lu
MOE International Joint Laboratory of Materials Microstructure
Institute for New Energy Materials and Low Carbon Technologies
School of Materials Science and Engineering
Tianjin University of Technology
Tianjin 300384, China
E-mail: luxiuli@email.tjut.edu.cn; lutongbu@tjut.edu.cn

S. Tao
School of Electronic and Information Engineering
Jiangsu Laboratory of Advanced Functional Materials
Changshu Institute of Technology
Changshu 215500, China

The ORCID identification number(s) for the author(s) of this article can be found under https://doi.org/10.1002/adma.202411942

DOI: 10.1002/adma.202411942

promoted protonation process.[24] Lu and co-workers fabricated an asymmetric TeN_2–CuN_3 double-atomic site catalyst for CO_2 electroreduction, in which Te center activates CO_2 and the Cu center helps to dissociate H_2O, bringing to efficient conversion of CO_2-to-CO.[25] These examples confirm the great advantage of dual metal sites in improving the activity of complicated electrocatalytic reactions. In this regard, fabricating efficient dual metal sites is a potential way to enhance the performance of Ru-based catalyst for alkaline water electrolysis. However, how to design and regulate dual metal sites on Ru-based catalysts for outstanding alkaline HER is still an open question. In addition, a multicomponent strategy is commonly used to solve the blockage of active sites during the catalytic process. It is reported that Pb-modified ultrathin RuCu nanoflowers can serve as highly active and stable catalysts for alkaline hydrogen oxidation reaction, in which Pb can act as an oxygen-rich site to accelerate CO oxidation and thus improve CO tolerance.[26] In our previous work, we revealed the unique role of oxygen vacancies in TiO_2 in V_O-rich Pt/TiO_2, which can boost the hydrogen spillover from Pt nanoclusters to TiO_2 support, avoiding the blockage of Pt active sites due to the accumulation of H* and accelerating the desorption process of H_2.[27]

For alkaline water electrolysis, the process of $^*OH + e^- \rightleftharpoons OH^-$ is usually sluggish, resulting in *OH blockage, which might not only reduce the catalytic activity but also destabilize the catalyst.[28,29] Thus, introducing competitive adsorption sites for *OH by multicomponent strategy is a potential way to transfer *OH during alkaline HER. On the basis of the above considerations, designing dual metal sites and multicomponent structure on Ru-based catalysts provide the opportunity for the realization of an efficient water dissociation process, fast transfer of adsorbed hydroxyl, and suitable hydrogen adsorption simultaneously. Herein, we demonstrate that the Ru–Sn dual sites and the SnO_2 heterojunction can bring to the highly efficient water dissociation, optimized hydrogen adsorption, and accelerated *OH transfer via hydroxyl spillover effect in Ru–Sn/SnO_2 NS, which results in an extremely low overpotential of 12 mV and excellent stability up to 650 h at 10 mA cm^{-2}. The Ru–Sn dual sites and rapid adsorbed hydroxyl transfer was confirmed by atomic resolution high-angle annular dark-field scanning transmission electron microscopy (HAADF-STEM), X-ray absorption fine structure (XAFS) spectroscopy, density functional theory (DFT) analysis and in situ infrared spectroscopy. Our work not only provides a new way to design both efficient and stable catalysts for alkaline HER but also gives deep insight into the mechanism of alkaline HER.

2. Results and Discussion

In this work, the Ru-based catalysts were prepared through the sacrificial templating method (Figure S1, Supporting Information). First, metal atoms (Ru^{3+} or Sn^{4+}) were introduced into the structure of g-C_3N_4 (CN) nanosheet (NS) through a simple dicyandiamide-blowing method.[30] By tuning the amount of Sn^{4+}, the precursors of Ru–CN, Ru/Sn–CN-1, and Ru/Sn-CN-2 were obtained (the synthesis details are given in the Experimental section). The X-ray diffraction (XRD) patterns of Ru–CN, Ru/Sn–CN-1, and Ru/Sn–CN-2 are similar to that of CN, and no peaks ascribed to Ru-based compound can be observed, demonstrating that the structure of CN remains unchanged (Figure S2, Supporting Information). The conditions for removing the CN skeleton were first investigated under air atmosphere, showing the optimal annealing temperature of 375 °C (Figure S3, Supporting Information). After annealing the precursors of Ru-CN, Ru/Sn-CN-1, and Ru/Sn-CN-2 at 375 °C for 5 h under ambient conditions, followed by a subsequent treatment at 300 °C for 1 h under 5% H_2/Ar atmosphere, Ru NS, Ru–Sn NS and Ru–Sn/SnO_2 NS were successfully obtained, respectively. The structure and morphological features of the as-synthesized materials were investigated by XRD, high-resolution transmission electron microscopy (HRTEM), and high-angle annular dark-field scanning transmission electron microscopy (HAADF-STEM). As shown in **Figure 1**a, all the XRD patterns of Ru NS, Ru–Sn NS, and Ru–Sn/SnO_2 NS display the diffraction peaks belonged to the hexagonal-close-packed (hcp) phase of Ru (JCPDS No. 06–0663). It can be found that the diffraction peaks associated with hcp-Ru in Ru–Sn NS and Ru–Sn/SnO_2 NS are slightly shifted to lower angles, suggesting that the lattice distortion after introducing Sn into the lattice of Ru. Remarkably, the peaks attributed to SnO_2 is clearly observed at the XRD patterns of Ru–Sn/SnO_2 NS, indicating the co-existence of Sn doped hcp-Ru and SnO_2 component in Ru–Sn/SnO_2 NS.

The TEM images of Ru NS, Ru–Sn NS, and Ru–Sn/SnO_2 NS (Figure 1b; Figures S5a and S6a, Supporting Information) display the nanosheet morphology with porous structure due to the removal of CN skeleton. As shown in Figure 1c, the HRTEM image and its corresponding selected area electron diffraction (SAED) (Figure S4, Supporting Information) of Ru NS shows the lattice fringe of 0.205 nm, corresponding to the (101) plane of hcp-Ru. Notably, the lattice distance of (101) plane in the HRTEM images and corresponding SAEDs for Ru–Sn NS (Figure S5b,c, Supporting Information) and Ru–Sn/SnO_2 NS (Figure 1f; Figure S6b, Supporting Information) are slightly larger than that of hcp-Ru due to the doping of Sn atoms in Ru lattice, corresponding with the results from the XRD. In addition, as revealed in Figure 1d, the atomic resolution HAADF-STEM image of Ru–Sn NS provides detailed atom arrangements and interplanar spacings along the Ru (101) planes. Interestingly, owing to the higher Z-contrast of Sn against Ru elements, the brighter spots, as highlighted by the red circles corresponding to Sn atoms could be visualized among Ru atoms directly, demonstrating the indeed existence of Ru–Sn dual metal sites. The atomic intensity profiles recorded along the rectangle depicted in Figure 1d demonstrate the presence of isolated Sn atoms with heightened intensities. Moreover, the corresponding elemental mapping (Figure S5d, Supporting Information) reveals the even distribution of Ru and Sn in the as-obtained Ru–Sn NS. For Ru–Sn/SnO_2 NS, the HRTEM image (Figure 1f) and its corresponding SAED (Figure S6b, Supporting Information) shows that in addition to the lattice associated with Sn doped Ru (101), the lattice spacing of 0.347 nm, which corresponds to (110) plane of SnO_2 is also clearly observed. Moreover, the atomic resolution HAADF-STEM image (Figure 1g) and corresponding elemental mapping (Figure 1h) for Ru–Sn/SnO_2 NS confirm the distinct heterojunction interface between single-atom Sn doped Ru nanosheet (Ru–Sn component) and SnO_2 nanosheet. As depicted in Figure 1i, the intensity profiles along the rectangle in Figure 1g clearly indicate the presence of Sn single-atom doped in Ru atoms. The results

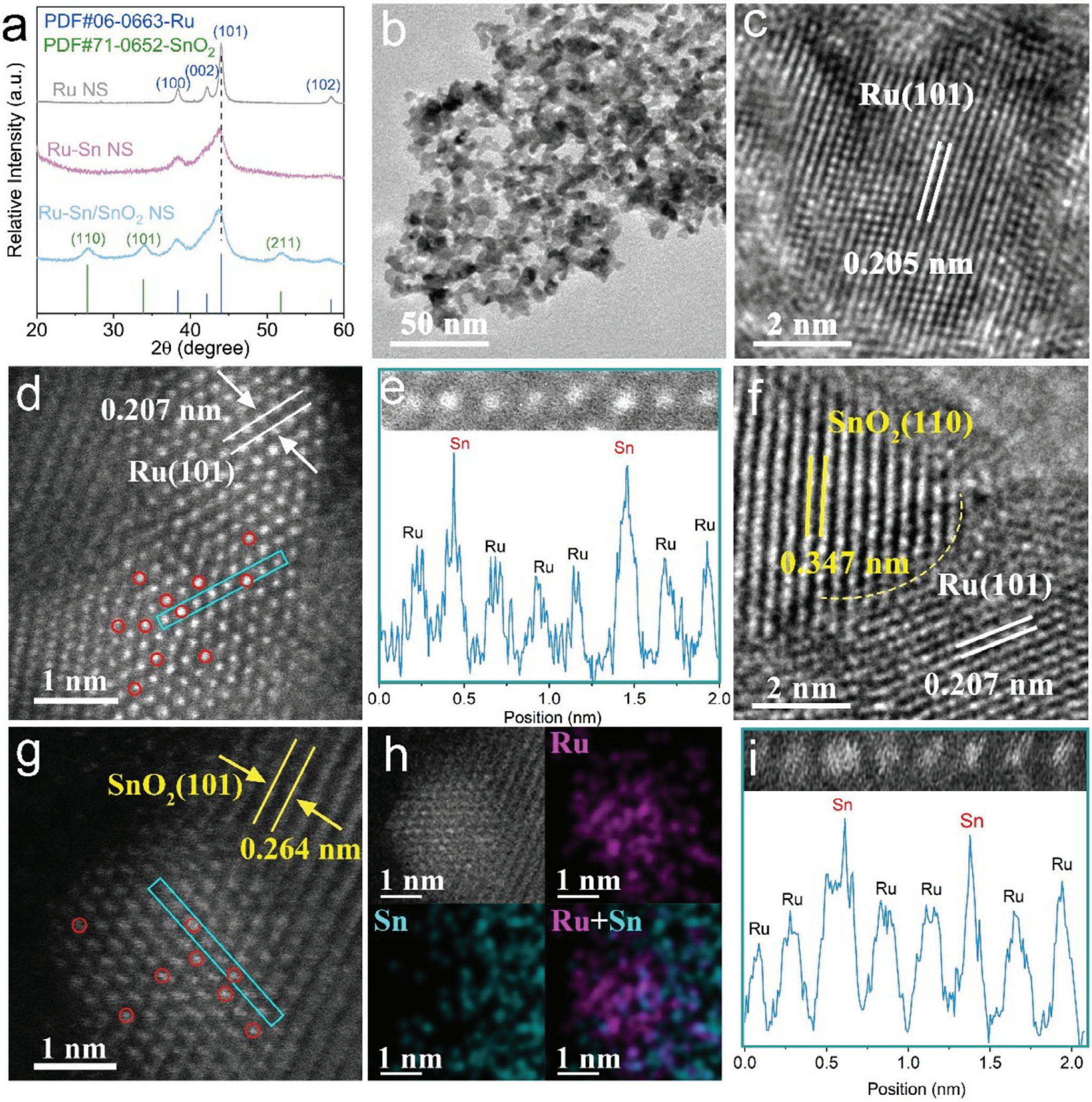

Figure 1. a) XRD patterns of Ru NS, Ru–Sn NS and Ru–Sn/SnO$_2$ NS. b) TEM image, and c) HRTEM image of Ru NS. d) The atomic resolution HAADF-STEM image of Ru–Sn NS (the Sn atoms were highlighted by the red circles). e) Line intensity profiles along the plane in (d). f) HRTEM image, g) the atomic resolution HAADF-STEM image (the Sn atoms were highlighted by the red circles), and h) the corresponding EDS element mapping for Ru–Sn/SnO$_2$ NS. i) Line intensity profiles along the plane in (g).

showcase the successful synthesis of Ru NS, Ru–Sn NS, and Ru–Sn/SnO$_2$ NS.

The electronic and structural information for Ru NS, Ru–Sn NS, and Ru–Sn/SnO$_2$ NS were further investigated by X-ray photoelectron spectroscopy (XPS) and X-ray absorption spectroscopy (XAS). As shown in Figure S7a (Supporting Information), the Ru $3p_{3/2}$ binding energies shift to more positive values in order of Ru NS, Ru–Sn NS, and Ru–Sn/SnO$_2$ NS, implying the increase in Ru valence states. In addition, the O1s XPS for Ru NS, Ru–Sn NS, and Ru–Sn/SnO$_2$ NS were also analyzed. As shown in **Figure 2a**, apart from the subpeaks attributed to surface adsorbed hydroxyl groups (530.25 eV), surface adsorbed H$_2$O (532.1 eV) and weakly bound oxygen species (533.6 eV), the O species related to Ru-O or Ru/Sn–O were also observed in the O 1s XPS of Ru NS and Ru–Sn NS,[31,32,34] respectively, indicating the O atoms were doped into Ru NS and Ru–Sn NS. In addition, the

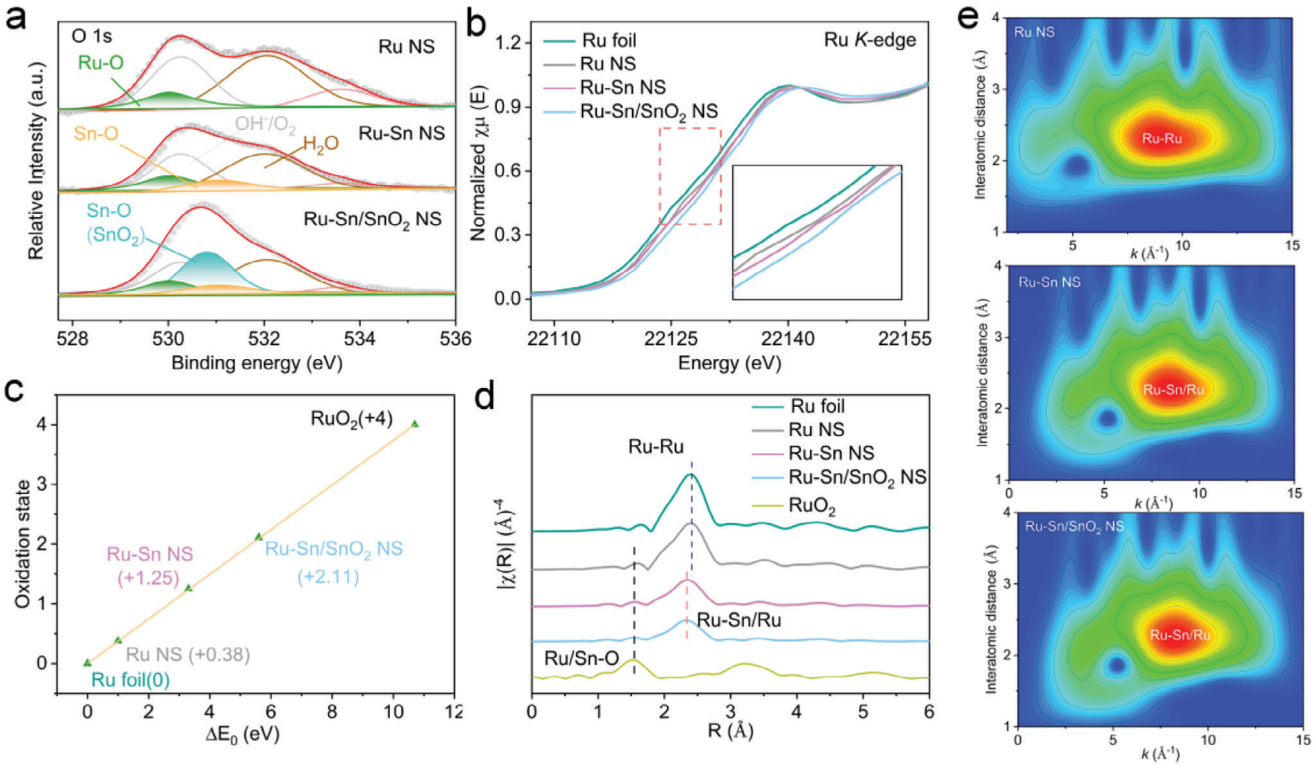

Figure 2. a) O1s XPS spectra for Ru NS, Ru–Sn NS and Ru–Sn/SnO_2 NS. b) Normalized Ru K-edge XANES of Ru foil, Ru NS, Ru–Sn NS and Ru–Sn/SnO_2 NS; c) the relation between the Ru K-edge absorption energy (ΔE_0) and oxidation states. d) Ru K-edge FT EXAFS spectra of Ru foil, Ru NS, Ru–Sn NS and Ru–Sn/SnO_2 NS, e) Wavelet transform-EXAFS spectra for Ru NS, Ru–Sn NS and Ru–Sn/SnO_2 NS.

extra subpeak at 530.8 eV related to the lattice O in SnO_2 also appears in the high-resolution XPS spectra of O 1s for Ru–Sn/SnO_2 NS.[35] The results indicate that O atoms were incorporated into the structure of Ru–Sn dual metal sites in both samples of Ru–Sn NS and Ru–Sn/SnO_2 NS, providing the possibility to balance the adsorption/desorption of hydroxyl species during alkaline HER. Moreover, as shown in Figure S7b (Supporting Information), the Sn 3d XPS spectra of Ru–Sn NS and Ru–Sn/SnO_2 NS display that the valence of Sn elements in Ru–Sn/SnO_2 NS is higher than that in Ru–Sn NS due to the existence of SnO_2 component. The Ru K edge spectra are further collected through X-ray absorption near-edge spectroscopy (XANES) to quantitatively describe the oxidation state of Ru (Figure 2b). As present in Figure 2c, taking Ru foil and commercial RuO_2 as references, the oxidation states of Ru in catalysts are estimated to be +0.38, +1.25, and +2.11 for Ru NS, Ru–Sn NS and Ru–Sn/SnO_2 NS, respectively, in line with the XPS results. It has been reported that high-valence Ru(n+) surfaces could promote interfacial water dissociation, promoting the alkaline HER.[8] To further reveal the structure of Ru–Sn dual metal sites in Ru–Sn NS and Ru–Sn/SnO_2 NS, the Ru K-edge Fourier transformed extended X-ray absorption fine structures (FT-EXAFS) are performed (Figure 2d), using Ru NS, Ru foil and commercial RuO_2 as references. It is worth noting that Ru–Sn NS and Ru–Sn/SnO_2 NS have characteristic peaks associated with Ru-Ru/Sn bonds. In addition, all the samples of Ru NS, Ru–Sn NS, and Ru–Sn/SnO_2 NS show the characteristic peaks related to Ru/Sn–O bonds. The fitting curves accord well with the experimental curves (Figure S8, Supporting Information), and the results were shown in Table S1 (Supporting Information). Additionally, the wavelet transform (WT) with high resolution in both k and R space analyses are carried out (Figure 2e), which is consistent with the FT-EXAFS results. The above results confirm that the dual Ru–Sn metal sites modified by O atoms were construed in both Ru–Sn NS and Ru–Sn/SnO_2 NS.

The HER performance of electrocatalyst of Ru–Sn/SnO_2 NS was evaluated in 1.0 M KOH aqueous solution with a typical three-electrode system, where a graphite counter electrode and a Hg/HgO reference electrode are applied. The Ru NS, Ru–Sn NS, commercial RuO_2, commercial Pt/C, commercial SnO_2, the mixture of Ru–Sn NS with commercial SnO_2 (denoted as "Ru–Sn NS + SnO_2"), and the precursors were also measured under the same conditions for comparison. As shown in **Figures** 3a and S9 (Supporting Information), the measured linear sweep voltammetry (LSV) curves show that Ru–Sn/SnO_2 NS displays the best catalytic performance for HER among those of Ru NS, Ru–Sn NS, commercial RuO_2 and commercial Pt/C, as well as the commercial SnO_2, the Ru–Sn NS + SnO_2 and the precursors. The overpotentials of different electrocatalysts were further compared in Figure 3b. Notably, extremely small overpotentials at 10 and 100 mA cm^{-2} were achieved in Ru–Sn/SnO_2 NS (12 and 72 mV) and Ru–Sn NS (16 and 93 mV) compared with those of Ru NS (27 and 120 mV), commercial Pt/C (27 and 135 mV) and commercial RuO_2 (128 and 232 mV). It's worth noting that the fabrication of Ru–Sn dual metal sites has improved the catalytic performance for HER. As shown in Figure 3c, both Ru–Sn/SnO_2 NS and

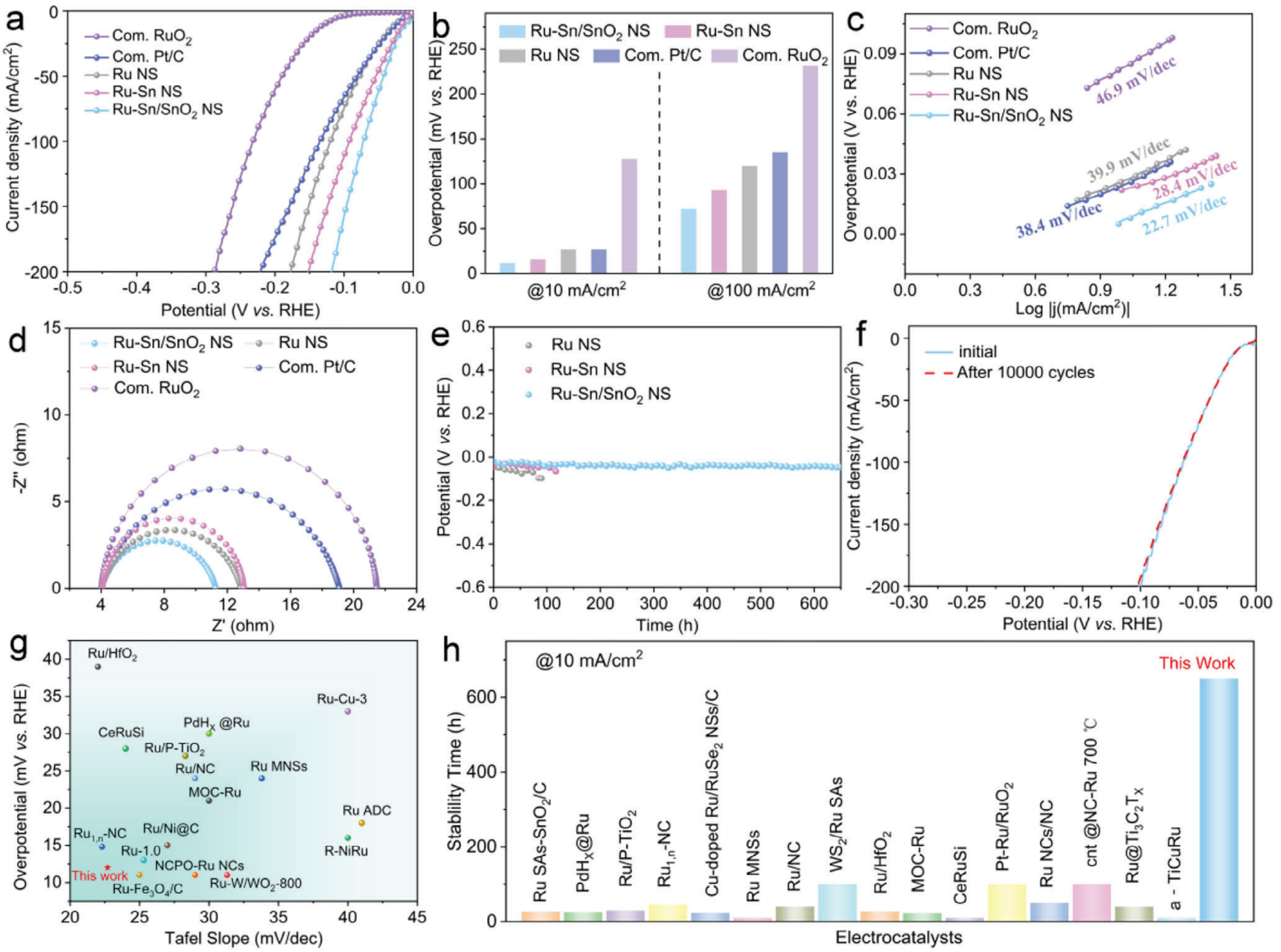

Figure 3. HER performance in 1 M KOH, a) LSV curves of Ru–Sn/SnO$_2$ NS, Ru–Sn NS, Ru NS, commercial Pt/C and commercial RuO$_2$ for HER. b) Comparing the overpotentials of above noted samples at the current density of 10 and 100 mA cm^{-2}. Tafel slopes c) and Nyquist plots d) for the above catalysts. e) Chronopotentiometry tests of Ru–Sn/SnO$_2$ NS, Ru–Sn NS and Ru NS at current densities of 10 mA cm^{-2}. f) HER polarization curves of Ru–Sn/SnO$_2$ NS before and after 10 000 CV cycles. g) Comparison of overpotential (η_{10}) and Tafel slope of Ru–Sn/SnO$_2$ NS with other representative Ru-based catalysts. h) Comparison of stability of Ru–Sn/SnO$_2$ NS with other representative Ru-based catalysts.

Ru–Sn NS obtain a lower Tafel slope (22.7 and 28.4 mV dec^{-1}) than that of Ru NS (39.9 mV dec^{-1}). In addition, Ru–Sn/SnO$_2$ NS exhibits the smallest charge-transfer resistance among all the catalysts, according to the electrochemical impedance spectroscopy (EIS) analysis (Figure 3d), demonstrating a faster HER kinetic process. Furthermore, as shown in Figure S10 (Supporting Information), the electrochemical double-layer capacitance C$_{\text{dl}}$ of Ru–Sn/SnO$_2$ NS is higher than that of Ru NS and Ru–Sn NS. This indicates that Ru–Sn/SnO$_2$ NS possesses a higher electrochemical active surface area (ECSA) than the other catalysts (Figure S11a,b, Supporting Information). In addition, the LSV curves normalized by ECSA display that Ru–Sn/SnO$_2$ NS remains the best performance for HER (Figure S11c, Supporting Information), suggesting the higher intrinsic electrocatalytic activity. This suggests that the Ru–Sn dual site and SnO$_2$ component could synergistically promote HER reaction kinetics. Furthermore, the stability of prepared electrocatalysts is further evaluated by long-term cyclic voltammetry (CV) cycling and chronoamperometry. As shown in Figure 3e, the chronopotentiometry test of Ru NS, Ru–Sn NS, and Ru–Sn/SnO$_2$ NS recorded at a fixed current density of 10 mA cm^{-2} demonstrates that the Ru–Sn/SnO$_2$ NS possess the best stability with no significant decline after 650 h electrolysis, much higher than those of Ru–Sn NS (120 h) and Ru NS (90 h). It is to say the introduction of SnO$_2$ component in Ru–Sn/SnO$_2$ NS could greatly improve the stability of the catalysts. Furthermore, the excellent stability of Ru–Sn/SnO$_2$ NS during alkaline HER were further proved by polarization curves, which were hardly changed after 10000 sweeping cycles (Figure 3f). It is noteworthy that Ru–Sn/SnO$_2$ NS demonstrates exceptional electrochemical performance, characterized by an impressively small Tafel slope, an exceptionally low overpotential, and remarkable long-term stability. These features position it as a superior alternative to the majority of recently reported advanced Ru-based catalysts, showcasing its great potential for applications requiring efficient and durable electrocatalytic activity. (Figure 3g,h; Tables S2 and S3, Supporting Information). In short, the above electrochemical results demonstrate that the Ru–Sn dual metal sites contribute more to the high activity of HER, while the SnO$_2$ component contribute more to the excellent stability of the catalysts in Ru–Sn/SnO_2 NS.

The morphology, compositional, and structural properties of Ru NS, Ru–Sn NS, and Ru–Sn/SnO_2 NS following the HER stability measurement in alkaline media have been further evaluated through SEM, TEM, XRD, and XPS analyses. As depicted in Figure S12 (Supporting Information), the powder XRD patterns of Ru–Sn NS and Ru–Sn/SnO_2 NS, post-HER stability testing, exhibit no discernible variations compared to the freshly prepared Ru–Sn NS and Ru–Sn/SnO_2 NS (Figure 1a). This observation shows that the structures for Ru–Sn NS and Ru–Sn/SnO_2 NS during HER are relatively stable. In contrast, after undergoing HER, Ru NS show a broadening of XRD peaks, indicating a lack of stability. In addition, as depicted in Figures S13a,b (Supporting Information) the binding energies of Ru $3p_{3/2}$ in both Ru NS and Ru–Sn NS exhibit a discernible shift toward more positive values subsequent to the HER stability measurement. This shift signifies an augmentation in the valence states of Ru, indicating that the Ru species within these nanostructures undergo oxidation to higher valence states during the HER process. This phenomenon aligns with previous reports in the literature.[36] In stark contrast to the observations in Ru NS and Ru–Sn NS, the Ru oxidation state in Ru–Sn/SnO_2 NS remains remarkably stable and unperturbed after the HER test, as evident from Figure S13c (Supporting Information). Concurrently, the Sn oxidation state in Ru–Sn/SnO_2 NS undergoes a shift to more positive values upon completion of the stability test, as confirmed by the Sn 3d XPS analysis presented in Figure S13d (Supporting Information). The observed increases in the valence states of Ru in Ru NS and Ru–Sn NS, as well as the increase in Sn valence states in Ru–Sn/SnO_2 NS, can be attributed to the adsorption of *OH species onto the Ru or Sn sites. These findings underscore the ability of hydroxyl groups to spillover from the Ru–Sn dual sites to the SnO_2 component. In addition, as presented in Figure S14 (Supporting Information), the SEM and TEM images demonstrate that the morphology of the Ru–Sn/SnO_2 NS remains intact and well-preserved during HER. Notably, the incorporation of SnO_2 within the Ru–Sn/SnO_2 NS framework plays a pivotal role in enhancing the long-term stability of the material, highlighting its crucial contribution to the overall performance.

To further unveil the mechanism of the superior alkaline HER catalytic activity of Ru–Sn/SnO_2 NS, the DFT calculations and in situ infrared spectroscopy were performed. Based on the above experimental results, the models of Ru, Ru-O, Ru–Sn, Ru–Sn–O, Ru–Sn/SnO_2 and Ru–Sn–O/SnO_2 (Figure S15, Supporting Information) were constructed to study the advantage of Ru–Sn dual metal sites for HER under alkaline conditions. As is known, facilitating slow water dissociation kinetics is the key to promoting the HER in alkaline condition. Given that, the energy barriers for the Vomer process were first calculated based on the fabricated models. As shown in **Figure 4**a, Figures S16a and S17–S22 (Supporting Information), the reaction energies associated with water dissociation on Ru model and Ru-O model are lower than those observed in other models incorporating Ru–Sn dual sites. However, the process of hydroxyl desorption on Ru model and Ru-O model face formidable obstacles stemming from uphill energy barriers (0.13 and 0.36 eV), which ultimately restrict the ability to achieve efficient and sustained water dissociation. For Ru–Sn model, while the initial water dissociation requires a small uphill energy barrier of 0.08 eV, the substantial downhill energy associated with hydroxyl desorption favors the progression of water dissociation, enhancing the efficiency of Volmer reaction (Figure S16a, Supporting Information). In addition, the downhill energies of Ru–Sn–O, Ru–Sn/SnO_2, and Ru–Sn–O/SnO_2 models for the Vomer process further indicate the high catalytic activity of Ru–Sn dual metal sites, especially modified by O atoms, for water splitting. Moreover, the advantage of Ru–Sn dual metal sites for water splitting was further investigated in D_2O/1 M KOH (Figure S23, Supporting Information). To evaluate the catalytic ability for H reduction, the H-adsorption free energy (ΔG_{H*}) were further calculated. As shown in Figure 4b and Figure S24 (Supporting Information), Ru–Sn–O/SnO_2 and Ru–Sn–O models exhibit the ΔG_{H*} value of −0.35 and −0.34 eV, which are closer to zero than that of Ru–O model (−0.37 eV), suggesting that the optimized adsorption of H and promoting the HER process. Moreover, as shown in Figure S16b (Supporting Information), the Ru–Sn/SnO_2 and Ru–Sn models also show a more suitable ΔG_{H*} value (−0.23 and −0.43 eV) compared with that of Ru model (−0.58 eV). In addition, the binding energies of OH on Ru and SnO_2 were also calculated and the results show that OH is more favorably adsorbed on the SnO_2 (Figure S25, Supporting Information). The strong interaction between SnO_2 and OH could induce the repaid hydroxyl spillover from the catalytic sites to SnO_2, solving the *OH blockage problem. As shown in Figure 4c, the hydroxyl spillover from site A to site B on Ru–Sn–O/SnO_2 model is effortless due to the large downhill energy. Thus, different from Ru NS and Ru–Sn NS, the desorption of adsorbed hydroxyl ($*OH + e^- \rightleftharpoons OH^-$) on Ru–Sn/$SnO_2$ NS preferred to occur on SnO_2 component, not on the catalytic sites, which could be used constantly for water splitting and H reduction.

To further investigate the catalytic process in Ru–Sn/SnO_2 NS during alkaline HER, the in situ attenuated total reflection surface-enhanced infrared absorption spectroscopy (ATR-SEIRAS) were conducted to monitor the $*H_2O$ and *OH. As shown in Figure S26 (Supporting Information), the broad peak from 3200−3600 cm^{-1} and the peaks located at ≈1621 cm^{-1} for Ru NS and Ru–Sn NS could be assigned to stretching (O—H) mode and the bending δ(H—O—H) mode of interfacial water molecules.[37] Under the same condition, the peaks related to water molecules for Ru–Sn/SnO_2 NS are more pronounced (Figure 4d,e), indicating enhanced water adsorption. Furthermore, a new small peak at ≈1144 cm^{-1} was found in the situ infrared spectra of Ru–Sn NS, which could be assigned to the Sn–OH stretching vibrations ($\delta_{Sn\text{-}OH}$).[38] This phenomenon confirms that the Sn atoms were more likely to adsorb OH in the Ru–Sn dual metal sites during the water splitting process. In addition to these small bands, the new bands attributed to the isolated terminal hydroxyl groups on the SnO_2 (υ_{Sn-OH}) at ≈3700 cm^{-1}[39] appear in the in situ infrared spectra for Ru–Sn/SnO_2 NS (Figure 4d,e). In addition, as the catalytic reaction proceeds, this band becomes more pronounced (Figure 4d). For comparison, the in situ ATR-SEIRAS were also conducted for commercial SnO_2 and Ru–Sn NS + SnO_2 at the potential of −160 mV versus RHE in 1 M KOH. As shown in Figure S27 (Supporting Information), no signal for υ_{Sn-OH} at ≈3700 cm^{-1} could be observed in SnO_2 and Ru–Sn NS + SnO_2, indicating that the OH^- from electrolyte does not impact the in situ infrared signal, and the heterojunction in Ru–Sn/SnO_2 NS is crucial for the

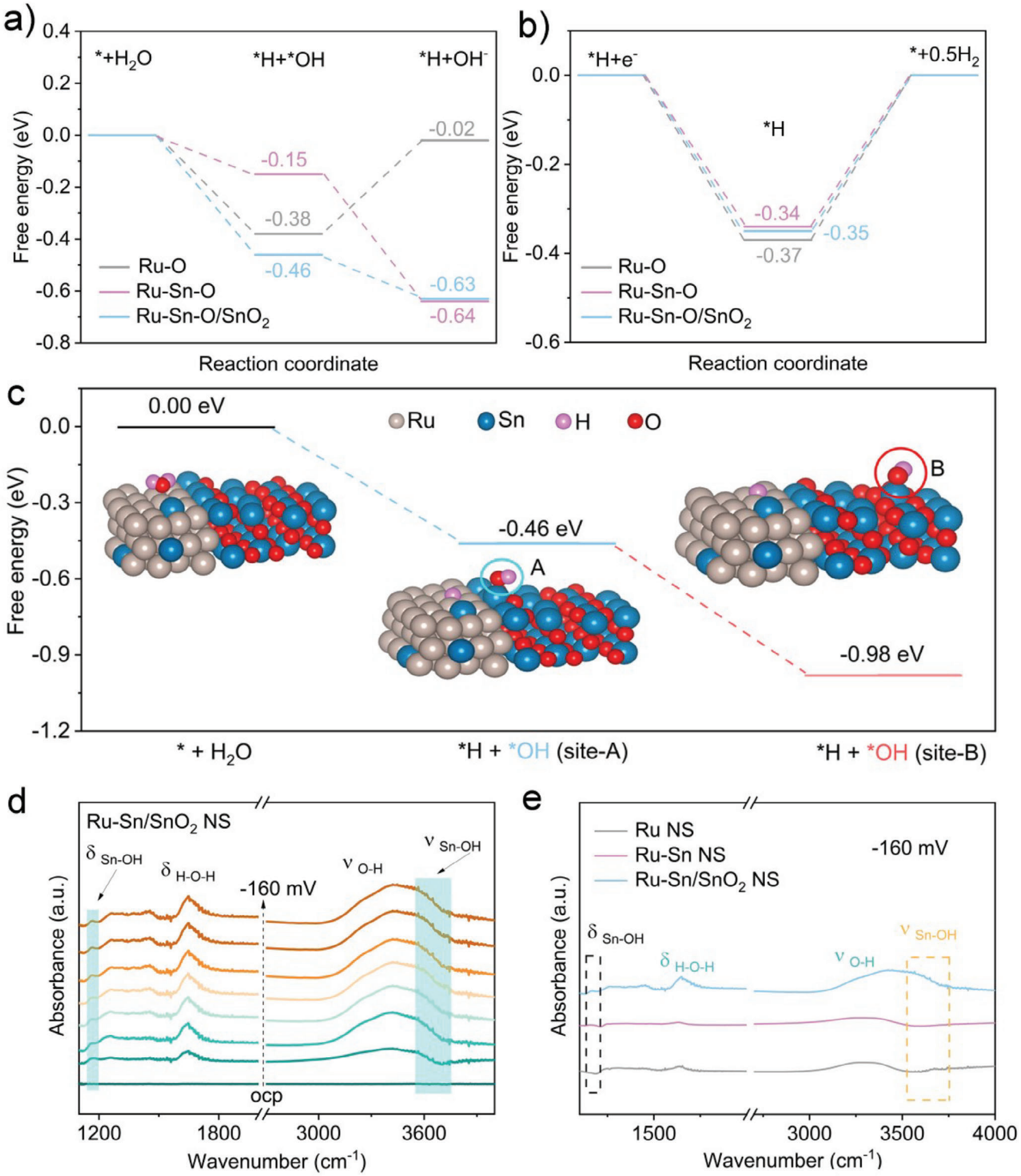

Figure 4. a) Free energy diagram for Vomer process. b) Free energy diagram for hydrogen recombination. c) Free energy diagram for hydroxyl spillover on Ru–Sn–O/SnO_2 model. d) The in situ infrared spectra of Ru–Sn/SnO_2 NS at different applied cathodic potentials during alkaline HER. e) Comparison of the in situ infrared spectra of Ru NS, Ru–Sn NS and Ru–Sn/SnO_2 NS at −160 mV versus RHE.

efficient hydroxyl spillover effect. The above in situ infrared spectra confirm that rapid *OH transfer does exist in Ru–Sn/SnO_2 NS during alkaline HER, and Ru–Sn dual metal sites act as the efficient catalytic sites for water splitting, thus synergistically promoting hydrogen generation.

3. Conclusion

In summary, we have successfully constructed a cooperative electrocatalyst of Ru–Sn/SnO_2 NS, in which Ru–Sn dual metal sites and SnO_2 combined together by forming the heterojunctions. The Ru–Sn/SnO_2 NS shows an outstanding electrocatalytic HER performance, with an extremely low overpotential (12 mV at 10 mA cm^{-2}) and robust stability (650 h at 10 mA cm^{-2}). The atomic HAADF-STEM image, XAFS spectra, XPS spectra, and DFT results confirm the Ru–Sn dual metal sites with O modification, which possess a low water splitting energy barrier and optimized adsorption of H. In addition, the results of DFT and in situ infrared revealed the role of SnO_2 component in Ru–Sn/SnO_2 NS, which can boost the *OH transfer from Ru–Sn dual metal sites to SnO_2 via novel hydroxyl spillover effect, further enhancing the HER activity and the stability of catalysts. This work provides important inspiration for designing highly efficient catalysts for alkaline HER.

Supporting Information

Supporting Information is available from the Wiley Online Library or from the author.

Acknowledgements

Z.T.Y., S.T., and J.W. contributed equally to this work. This work was supported by the National Natural Science Foundation of China (No.21931007, No.21805207), the National Key Research and Development Program of China (No.2022YFA1502902), and the Natural Science Foundation of the Jiangsu Higher Education Institutions (No.23KJA430001).

Conflict of Interest

The authors declare no conflict of interest.

Data Availability Statement

The data that support the findings of this study are available in the supplementary material of this article.

Keywords

alkaline hydrogen evolution reaction, dual metal sites, heterojunction, hydroxyl spillover effect, Ru-based catalysts

Received: August 13, 2024
Revised: September 14, 2024
Published online:

[1] S. Anantharaj, S. Noda, V. R. Jothi, S. Yi, M. Driess, P. W. Menezes, *Angew. Chem., Int. Ed.* **2021**, *60*, 18981.

[2] B. E. Logan, L. Shi, R. Rossi, *Joule* **2021**, *5*, 760.

[3] G. Li, H. Jang, S. Liu, Z. Li, M. G. Kim, Q. Qin, X. Liu, J. Cho, *Nat. Commun.* **2022**, *13*, 1270.

[4] W. Cai, C. Zhou, X. Hu, T. Jiao, Y. Liu, L. Li, J. Li, M. Kitano, H. Hosono, J. Wu, *ACS Catal.* **2023**, *13*, 4752.

[5] Y. Zuo, S. Bellani, G. Saleh, M. Ferri, D. V. Shinde, M. I. Zappia, J. Buha, R. Brescia, M. Prato, R. Pascazio, A. Annamalai, D. O. de Souza, L. De Trizio, I. Infante, F. Bonaccorso, L. Manna, *J. Am. Chem. Soc.* **2023**, *145*, 21419.

[6] A. H. Shah, X. Pan, T. Hu, A. N. Alexandrova, Y. Huang, X. Duan, *Nat. Mater.* **2023**, *22*, 1022.

[7] X. Lin, W. Hu, J. Xu, X. Liu, W. Jiang, X. Ma, D. He, Z. Wang, W. Li, L. M. Yang, H. Zhou, Y. Wu, *J. Am. Chem. Soc.* **2024**, *146*, 4883.

[8] X. Chen, X. T. Wang, J. B. Le, S. M. Li, X. Wang, Y. J. Zhang, P. Radjenovic, Y. Zhao, Y. H. Wang, X. M. Lin, J. C. Dong, J. F. Li, *Nat. Commun.* **2023**, *14*, 5289.

[9] a) Y. Dai, H. C. Fu, X. H. Chen, Q. Zhang, T. Li, N. B. Li, H. Q. Luo, *Chem. Eng. J.* **2023**, *475*, 146443; b) X. Guo, X. Wan, Q. Liu, Y. Li, W. Li, J. Shui, *eScience* **2022**, *2*, 304.

[10] a) A. Kong, M. Peng, M. Liu, Y. Lv, H. Zhang, Y. Gao, J. Liu, Y. Fu, W. Li, J. Zhang, *Appl. Catal., B.* **2022**, *316*, 121654; b) Y. Sun, X. Li, T. Zhang, K. Xu, Y. Yang, G. Chen, C. Li, Y. Xie, *Angew. Chem., Int. Ed.* **2021**, *60*, 21575.

[11] J. Wang, S. Xin, Y. Xiao, Z. Zhang, Z. Li, W. Zhang, C. Li, R. Bao, J. Peng, J. Yi, S. Chou, *Angew. Chem., Int. Ed.* **2022**, *61*, 202202518.

[12] a) J. Wu, J. Fan, X. Zhao, Y. Wang, D. Wang, H. Liu, L. Gu, Q. Zhang, L. Zheng, D. J. Singh, X. Cui, W. Zheng, *Angew. Chem., Int. Ed.* **2022**, *61*, e202207512; b) Q. Hu, J. Wang, X. Zheng, X. Han, Y. Deng, W. Hu, Z. Chen, *Sci. China Mater.* **2022**, *65*, 1825.

[13] J. Xu, X. Wang, X. Mao, K. Feng, J. Xu, J. Zhong, L. Wang, N. Han, Y. Li, *Energy Environ. Sci.* **2023**, *16*, 6120.

[14] H. Ren, Z. Zhang, Z. Geng, Z. Wang, F. Shen, X. Liang, Z. Cai, Y. Wang, D. Cheng, Y. Cao, X. Yang, M. Hu, X. Yao, K. Zhou, *Adv. Energy Mater.* **2024**, *14*, 2400777.

[15] X. Chen, C. Chen, M. M. Amjad, D. Sun, B. Sun, K. Zhang, *Appl. Catal., B: Environ. Energy* **2024**, *344*, 123644.

[16] Y. Yang, Y. Yu, J. Li, Q. Chen, Y. Du, P. Rao, R. Li, C. Jia, Z. Kang, P. Deng, Y. Shen, X. Tian, *Nano-Micro Lett.* **2021**, *13*, 160.

[17] W. Xi, L. Jin, A. Mahmood, W. Zhang, Y. Li, H. Li, P. An, J. Zhang, T. Ma, S. Liu, J. Yan, *Adv. Energy Mater.* **2023**, *13*, 2302668.

[18] J. Zhang, G. Chen, Q. Liu, C. Fan, D. Sun, Y. Tang, H. Sun, X. Feng, *Angew. Chem., Int. Ed.* **2022**, *61*, e202209486.

[19] W. Sheng, M. Myint, J. G. Chen, Y. Yan, *Energy Environ. Sci.* **2013**, *6*, 1509.

[20] Q. He, Y. Zhou, H. Shou, X. Wang, P. Zhang, W. Xu, S. Qiao, C. Wu, H. Liu, D. Liu, S. Chen, R. Long, Z. Qi, X. Wu, L. Song, *Adv. Mater.* **2022**, *34*, 2110604.

[21] S. Zhu, Z. Li, L. Hou, M. G. Kim, H. Jang, S. Liu, X. Liu, *Adv. Funct. Mater.* **2024**, *34*, 2314899.

[22] K. Wang, J. Zhou, M. Sun, F. Lin, B. Huang, F. Lv, L. Zeng, Q. Zhang, L. Gu, M. Luo, S. Guo, *Adv. Mater.* **2023**, *35*, 2300980.

[23] F. Shen, Z. Zhang, Z. Wang, H. Ren, X. Liang, Z. Cai, S. Yang, G. Sun, Y. Cao, X. Yang, M. Hu, Z. Hao, K. Zhou, *Nat. Commun.* **2024**, *15*, 448.

[24] D. Wang, X. Zhu, X. Tu, X. Zhang, C. Chen, X. Wei, Y. Li, S. Y. Wang, *Adv. Mater.* **2023**, *35*, 2304646.

[25] J. J. Jiao, Q. Yuan, M. Tan, X. Han, M. Gao, C. Zhang, X. Yang, Z. Shi, Y. B. Ma, H. Xiao, J. Zhang, T. B. Lu, *Nat. Commun.* **2023**, *14*, 6164.

[26] Y. Dong, Z. Zhang, W. Yan, X. Hu, C. Zhan, Y. Xu, X. Huang, *Angew. Chem., Int. Ed.* **2023**, *62*, e202311722.

[27] Z. W. Wei, H. J. Wang, C. Zhang, K. Xu, X. L. Lu, T. B. Lu, *Angew. Chem., Int. Ed.* **2021**, *60*, 16622.
[28] R. Yao, K. Sun, K. Zhang, Y. Wu, Y. Du, Q. Zhao, G. Liu, C. Chen, Y. Sun, J. Li, *Nat. Commun.* **2024**, *15*, 2218.
[29] L. Wang, M. Ma, C. Zhang, H. H. Chang, Y. Zhang, L. Li, H. Y. Chen, S. Peng, *Angew. Chem., Int. Ed.* **2024**, *63*, e202317220.
[30] S. F. Tang, X. P. Yin, G. Y. Wang, X. L. Lu, T. B Lu, *Nano Res.* **2019**, *12*, 457.
[31] Z. Hu, X. Liu, D. Meng, Y. Guo, Y. Guo, G. Lu, *ACS Catal.* **2016**, *6*, 2265.
[32] C. Rong, X. Shen, Y. Wang, L. Thomsen, T. Zhao, Y. Li, X. Lu, R. Amal, C. Zhao, *Adv. Mater.* **2022**, *34*, 2110103.
[33] C. Li, S. H. Kim, H. Y. Lim, Q. Sun, Y. Jiang, H. J. Noh, S. J. Kim, J. Baek, S. K. Kwak, J. B. Baek, *Adv. Mater.* **2023**, *35*, 2301369.
[34] Y. Zhu, M. Klingenhof, C. Gao, T. Koketsu, G. Weiser, Y. Pi, S. Liu, L. Sui, J. Hou, J. Li, H. Jiang, L. Xu, W. H. Huang, C. W. Pao, M. Yang, Z. Hu, P. Strasser, J. Ma, *Nat. Commun.* **2024**, *15*, 1447.
[35] V. Bonu, A. Das, M. Sardar, S. Dhara, A. K. Tyagi, *J. Mater. Chem. C.* **2015**, *3*, 1261.
[36] S. Yan, X. Chen, W. Li, M. Zhong, J. Xu, M. Xu, C. Wang, N. Pinna, X. Lu, *Adv. Sci.* **2024**, *11*, 2307061.
[37] X. Ding, R. Jiang, J. Wu, M. Xing, Z. Qiao, X. Zeng, S. Wang, D. Cao, *Adv. Funct. Mater.* **2023**, *33*, 2306786.
[38] W. Wan, Y. Li, X. Ren, Y. Zhao, F. Gao, H. Zhao, *Nanomaterials* **2018**, *8*, 112.
[39] K. Khamfoo, A. Staerz, M. Boepple, A. Wisitsoraat, C. Liewhiran, U. Weimar, N. Barsan, *Sens. Actuators, B.* **2022**, *371*, 132495.